Materials Research Bulletin 127 (2020) 110860

Contents lists available at ScienceDirect

Materials Research Bulletin

journal homepage: www.elsevier.com/locate/matresbu

# Synthesis, structural and optical properties of mesostructured, X-doped NiO (x = Zn, Sn, Fe) nanoflake network films

M.H. Mamat[a,b,*], N. Parimon[a], A.S. Ismail[a], I.B. Shameem Banu[c], S. Sathik Basha[c], R.A. Rani[b], A.S. Zoolfakar[a], M.F. Malek[b,d], A.B. Suriani[e], M.K. Ahmad[f], M. Rusop[a,b]

[a] NANO-ElecTronic Centre (NET), Faculty of Electrical Engineering, Universiti Teknologi MARA (UiTM), 40450, Shah Alam, Selangor, Malaysia
[b] NANO-SciTech Centre (NST), Institute of Science (IOS), Universiti Teknologi MARA (UiTM), 40450, Shah Alam, Selangor, Malaysia
[c] Department of Physics, B.S. Abdur Rahman Crescent Institute of Science & Technology, Vandalur, Chennai, 600 048, India
[d] Faculty of Applied Sciences, Universiti Teknologi MARA (UiTM), 40450, Shah Alam, Selangor, Malaysia
[e] Nanotechnology Research Centre, Faculty of Science and Mathematics, Universiti Pendidikan Sultan Idris (UPSI), 35900 Tanjung Malim, Perak, Malaysia
[f] Microelectronic and Nanotechnology – Shamsuddin Research Centre (MiNT-SRC), Faculty of Electrical and Electronic Engineering, Universiti Tun Hussein Onn Malaysia (UTHM), 86400 Batu Pahat, Johor, Malaysia

ARTICLE INFO

*Keywords:*
NiO
Nanoflake network film
Solution immersion
Optical properties
Structural properties

ABSTRACT

Mesostructured nickel oxide (NiO) nanoflake network films doped with zinc (Zn), tin (Sn), and iron (Fe), were grown by a one-step solution immersion method at 120$^0$C on indium-doped tin oxide (ITO) glass substrates. Field emission scanning electron microscope images revealed that the NiO nanoflake networks doped with Zn, Sn, and Fe, grew on the ITO but with different nanoflake morphologies and thicknesses, and their growth mechanisms are discussed. The X-ray diffraction patterns show that all grown films exhibited polycrystalline NiO structures. Substantial modifications and anomalies in the NiO film's morphology, thickness, lattice constant, stress/strain, crystallite size, and dislocation density, were observed when doped with the different sources. The optical and electrical properties also altered after the doping process. The Raman spectra indicated that all the films exhibited cubic NiO structures with paramagnetic characteristics. Moreover, the characteristic deviations in the doped NiO nanoflake network films have been thoroughly discussed.

## 1. Introduction

Nickel oxide (NiO) is a p-type metal oxide semiconductor with a wide band gap energy of 3.6–4 eV. Generally, NiO exhibits both rhombohedral and cubic structures. However, its lattice structure is dominated by the cubic structure [1]. The p-type conductivity of NiO is attributed to the cation deficit or Ni vacancies in the lattice. Recently, this binary oxide has attracted much attention in many applications such as solar cells, batteries, sensors, energy storage, and memory devices [2–7]. There are many techniques that have been applied to fabricate NiO either in powder structures or films, including spray pyrolysis, sputtering, hydrothermal, and solution-based methods [8–12]. Particularly for the preparation of NiO nanostructures, the solution-based method offers plenty of advantages including low-cost processing, simplicity of the fabrication process, and the ability to produce high quality nanomaterials.

A doping process with metal elements has been regarded as one of effective approaches to modify the NiO properties. It has been reported that the doped NiO shows enhanced sensing performance and improved energy storage capacity [13,14]. Therefore, the optimization of the doping process, including the selection of suitable dopant materials, is very crucial to improving the NiO properties. Recently, a few metal sources, which include indium, tin, manganese, iron, and cobalt, have been used as dopants in NiO [15–18]. Each dopant alters the NiO characteristics when it is incorporated into the NiO lattice, and these characteristic variations are very useful for different kinds of applications. However, the characteristics of the doped NiO are also significantly influenced and controlled by the preparation methods and their corresponding parameters. In other words, NiO prepared by different methods but with similar dopants might exhibit different characteristics. Therefore, it is difficult to compare and evaluate the conclusive impact of the various dopants on the properties of NiO based on the reported works due to variances of the methods and parameters used to prepare the doped NiO. Each method might have different

* Corresponding author at: NANO-ElecTronic Centre (NET), Faculty of Electrical Engineering, Universiti Teknologi MARA (UiTM), 40450, Shah Alam, Selangor, Malaysia.
*E-mail address:* mhmamat@uitm.edu.my (M.H. Mamat).

https://doi.org/10.1016/j.materresbull.2020.110860
Received 25 November 2018; Received in revised form 17 January 2020; Accepted 17 March 2020
Available online 19 March 2020

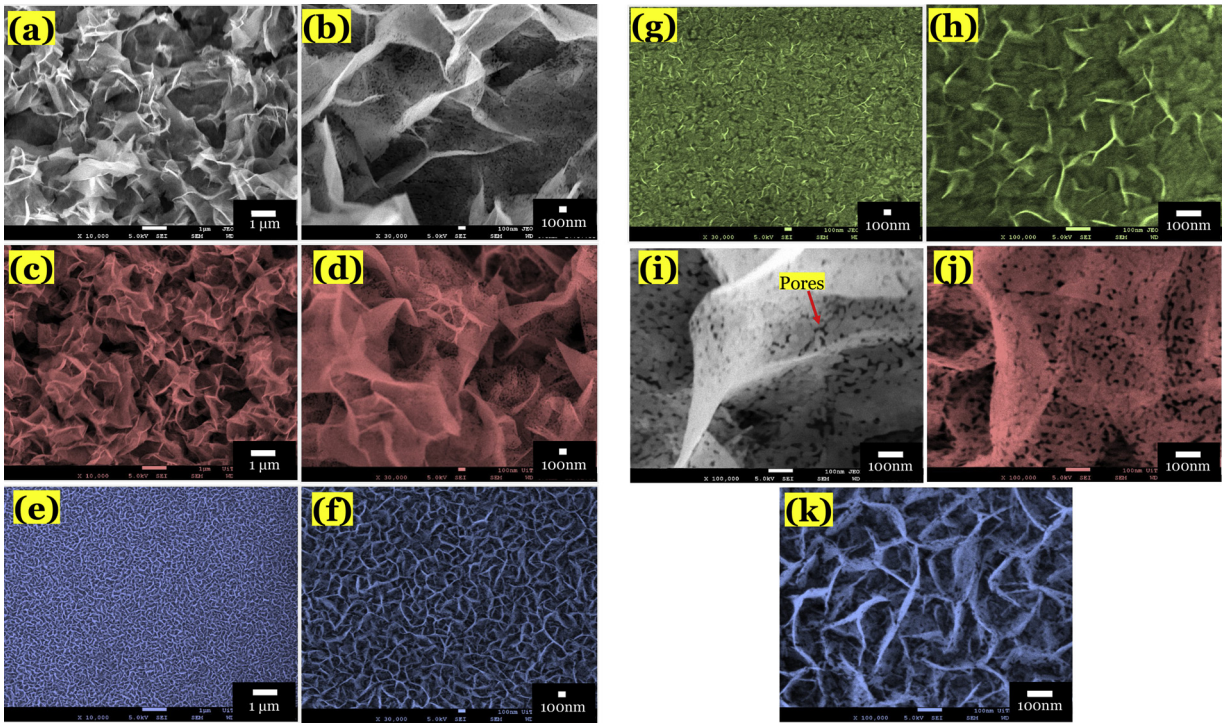


**Fig. 1.** Typical FESEM images of mesostructured NiO nanoflake network films at low and high magnifications; (a-b) Undoped (UNF); (c-d) Zn-doped (ZNF); (e-f) Sn-doped (SNF); and (g-h) Fe-doped (FNF). Magnified images (at 100,000× magnification) of (i) UNF, (j) ZNF, and (k) SNF.

kinetics and mechanisms of the doping process, which leads to different characteristics of the doped samples. In addition, most of the literature relates to the properties of doped NiO films with dense granular structure, and to the properties of doped NiO nanostructures in powder form structure [19–22]. However, reports and discussions on the doped NiO nanostructured films, which are directly grown or deposited on the substrate, based on one-step methods, are still lacking.

Herein, the one-step solution immersion method was utilized to directly grow undoped and doped NiO nanoflake network films on ITO glass substrates. The influence of doping with zinc (Zn), tin (Sn), and iron (Fe), on the optical and structural anomalies of the network films were thoroughly investigated. This study provides distinct and complementary data to the current literature because it permits a direct comparison between the undoped and doped samples, particularly for NiO nanoflake network films grown on the substrate based on a one-step solution immersion approach, as they were grown using the same parameters and immersion vessel, changing only the dopant materials. To the best of our knowledge, there are few reports on the structural and optical properties of NiO nanoflake network films with different dopants (i.e., Zn, Sn, and Fe), particularly on nanoflake network films that are grown directly on the substrate using a one-step solution immersion method.

## 2. Experimental procedure

Undoped and doped NiO nanoflake network films were prepared by the solution immersion method onto indium-doped tin oxide (ITO) glass substrates (commercially purchased, resistivity 15 Ω·cm, thickness: 200 nm) at 120$^0$C. A solution for the undoped sample was prepared using 0.1 M nickel (II) nitrate hexahydrate as a precursor, and 0.1 M hexamethylenetetramine (HMT) as a stabilizer, which were dissolved in a beaker filled with deionized (DI) water. Doping was achieved by adding 0.001 M zinc nitrate hexahydrate, 0.001 M tin chloride dihydrate, and 0.001 M iron chloride hexahydrate into three separate undoped solutions to attain Zn-, Sn-, and Fe-doped solutions, respectively. Each solution was sonicated for 5 min using an ultrasonic bath to improve their miscibility. After that, the solution was transferred into a Schott bottle. Inside the Schott bottle, the ITO glass substrate was positioned at the bottom with the conductive ITO layer facing upwards. Then, the bottle was tightly closed with its cap before being inserted into an oven at 120 °C for 2 h. After the immersion process, the grown nanostructured NiO on the ITO glass was rinsed with DI water and successively baked in the furnace at 150$^0$C for 10 min. Subsequently, the sample was annealed at 500$^0$C for 1 h in an ambient atmosphere. The resulting undoped, Zn-doped, Sn-doped, and Fe-doped NiO nanoflake network films are abbreviated as UNF, ZNF, SNF, and FNF, respectively.

The surface morphology and cross-sectional images of the grown undoped and doped films were analyzed by field-emission scanning electron microscopy (FESEM; JEOL JSM-7600 F). The crystallinity of the samples was investigated using X-ray diffraction (XRD; PANalytical X'Pert PRO). The X-ray profile of standard highly crystalline lanthanum hexaboride was used to make instrumental broadening corrections. The optical transmittance measurements of the samples, in the ultraviolet-visible (UV–vis) range, were carried out using UV–vis double-beam spectroscopy (Perkin Elmer Lambda 750). The Raman spectra measurements of the samples were conducted at room temperature using micro-Raman spectroscopy (Horiba Jobin Yvon-79DU420A-OE-325). The Raman spectra were obtained using a 514-nm argon (Ar) laser as an excitation source. The current-voltage (I–V) measurements were conducted at room temperature using a two-probe I–V measurement system (Keysight B1500A). To measure the I–V, 60-nm-thick Platinum (Pt) was used as an electrode and ITO (from the substrate) was used as a counter electrode. The Pt electrodes were deposited on the films using an electron beam evaporator (Ulvac).

## 3. Results and discussion

The FESEM images of the UNF, ZNF, SNF, and FNF, prepared using the solution immersion method, are shown in Figs. 1(a)–(h). These morphological images reveal that the mesostructured NiO nanoflake network grew uniformly on the ITO glass after immersion for 2 h. The FESEM images also reveal that the nanoflake morphology of the NiO

exhibits a considerable change after doping with different sources. The UNF sample in Fig. 1 (a) exhibits a nanoflake network morphology with a large nanoflake structure. A higher magnification FESEM image, in Fig. 1(b), shows that the UNF has a very thin nanoflake mesostructure, which has nanopores on the surface. These nanoflakes linked up to the adjacent nanoflakes and simultaneously accumulated to form a nanoflake network film. Meanwhile, the ZNF sample in Fig. 1(c) shows an almost similar surface structure as UNF but with a denser morphology. The ZNF also possess nanopores on the surface, which can be observed in the higher magnification image in Fig. 1(d). The nanopores are formed on the nanoflake as a result of aggregation between small NiO particles. However, the morphology of NiO is significantly changed when doped with Sn as shown for the SNF sample in Fig. 1(e). This morphology is dissimilar from that obtained for the UNF and ZNF samples, in that it exhibits a comparatively dense structure with small nanoflakes. The nanoflake size was substantially reduced as compared to the UNF and ZNF samples. The morphology of the nanoflake network for SNF can be clearly observed with high uniformity in the magnified image in Fig. 1(f). Another apparent feature of SNF is the presence of an ordered and dense nanoflake network structure. The surface morphology for FNF is shown in Fig. 1(g). For the FNF sample, the images were taken at higher magnification because the morphology could not be clearly observed in low magnification images. The image shows that that the nanoflake network structure for FNF was more irregular as compared to other samples. The sample also exhibits a nanoflake structure with small dimensions, as evidenced in the higher FESEM image in Fig. 1(h). Similarly, high magnification images (at 100,000×) of UNF, ZNF, and SNF samples were taken and are shown in Figs. 1(i), 1(j), and 1(k), respectively. The magnified images of the samples clearly show that the two-dimensional NiO nanoflake was constructed from a series of NiO nanocrystallite chains. These small crystallite chains produce a unique and mesoporous nanoflake structure with a pore diameter less than 50 nm. The pores are represented by the black dots, as labelled in Fig. 1(i). The morphologies of the undoped and doped NiO nanoflakes also exhibit some irregular structures, which are due to the thermodynamic instability of the formed NiO nuclei that have a high interfacial energy during nucleation. As the growth reaction proceeds, the morphology and quantity of the nuclei continuously improves to create more NiO crystallites, which subsequently combine with each other and develop into the nanoflake structure.

The FESEM cross-sectional images of UNF, ZNF, SNF, and FNF are shown in Figs. 2 (a)-(d). The image in Fig. 2(a) shows that the UNF grew on the ITO substrate, in which the nanoflakes formed multiple networks with each other creating a porous film. It can be observed in this Figure that a dense film with a small nanoflake network structure was preliminary grown on the ITO, followed by a large and predominant nanoflake network layer on top of the dense layer. This condition indicates that the dense NiO layer, which has a thickness of approximately 200 nm, was initially grown on the ITO to act as an epilayer, or a seed layer, that provides increased surface energy for the subsequent nanoflake growth. The thickness of the UNF film is approximately 4.2 μm. The presence of this dense layer was also observed for the ZNF and SNF samples but with a smaller thickness, as depicted in Figs. 2(b) and (c), respectively. The film thickness for the ZNF film was estimated to be 3.5 μm, whereas the thickness of the SNF film was approximately 2.1 μm. However, for the FNF sample, it is difficult to observe this dense layer due to a small film thickness of 250 nm, as shown in the cross-sectional image in Fig. 2(d).

From the FESEM images, it can be concluded that generally, the introduction of dopants retards the growth of the nanoflake film on the ITO substrate due to the reduction of the nucleation ions. The dopants might also be predominantly present on the nanoflake surface which hinders the crystal growth, which explains the reduction in thickness and nanoflake size for the doped samples. This condition is possible since the enthalpies of formation for these metal dopants to form oxides are smaller than that of NiO. The enthalpies of formation for NiO, ZnO, $SnO_2$, and $Fe_2O_3$, are -240 kJmol$^{-1}$, -324 kJmol$^{-1}$, -578 kJmol$^{-1}$, and -740 kJmol$^{-1}$, respectively [23–26]. Therefore, these dopants are presumably incorporated at an early stage of the nanoflake growth and change the free energy of the system, which disturbs the formation of large nanoflakes inside the film. According to these enthalpies of formation, the Fe dopant is easily assimilated in the NiO nanoflake at an early stage of the growth as a result of the low enthalpy value, which impedes the consecutive growth of the nanoflake due to the deterioration of lattice structure induced by Fe doping. This is also the case for the SNF sample, where the addition of Sn dopant literally obstructs the nanoflake growth to produce a smaller size than those of the undoped sample. Zn dopant also produces a smaller nanoflake size but not as small as the size of the SNF sample, which is attributed to its large enthalpy of formation compared to those of the other dopants. Consequently, according to our results, the FNF sample shows the thinnest and most irregular nanostructures, followed by SNF, ZNF and UNF.

It has been reported that metal oxides with diverse morphologies can be grown using an appropriate metal salt in the solution [27,28]. The HMT was used in this study because it can act as a complex agent and provides alkaline conditions for NiO growth. Generally, the HMT dissolves in DI water to produce ammonia and formaldehyde according to the equation below:

$$(CH_2)_6N_4 + 6H_2O \rightarrow 6HCHO + 4NH_3 \quad (1)$$

The produced ammonia reacts with the precursor's $Ni^{2+}$ ion and forms complex ions of $[Ni(NH_3)_6]^{2+}$. This reaction reduces the precursor's $Ni^{2+}$ ion concentration and subsequently decreases the growth rate of NiO crystals in the solution. The reaction can be described as follows:

$$Ni(NO_3)_2{\cdot}6H_2O + 6NH_3 \rightarrow [Ni(NH_3)_6]^{2+} + 2NO_3^- + 6H_2O \quad (2)$$

Meanwhile, some of the ammonia reacts with the water and increases the concentration of OH- ions in the solution as the reaction continues. This reaction is shown as follows:

$$NH_3 + H_2O \rightarrow NH_4^+ + OH^- \quad (3)$$

When the concentration of $OH^-$ ions is sufficient for the solution to reach supersaturation, the $[Ni(NH_3)_6]^{2+}$ and/or $Ni^{2+}$ ions will react with $OH^-$ ions to form NiO as shown below:

$$[Ni(NH_3)_6]^{2+} + 2OH^- \rightarrow Ni(OH)_2 + 6NH_3 \rightarrow NiO + H_2O + 6NH_3 \quad (4)$$

and/or

$$Ni^{2+} + 2OH^- \rightarrow Ni(OH)_2 \rightarrow NiO + H_2O \quad (5)$$

Subsequently, the NiO nuclei are formed and assembled on the ITO glass when the supersaturation level in the solution surpasses its critical value. The nanoflake morphology is controlled by the adsorption of unreacted HMT on certain plane orientations of NiO, particularly the (001) plane, to direct the growth towards the thin nanoflake structure [29]. The adsorbed HMT prevents the precursor ions from attaching to these adsorbed-HMT-planes, thereby, the growth on the other planes could be enhanced to yield the nanoflake structure. From the FESEM image observations, the dense nanoflake layer was formed initially on the ITO glass due to the homogenization of the precursor ions and other reactants in the solution. This condition produces a high density of NiO nuclei grown on the ITO glass. As the reactions proceed, larger nanoflakes are formed and assembled to produce the nanoflake network film. The schematic for the growth of the NiO nanoflake film is depicted in Fig. 3.

The crystalline properties of UNF, ZNF, SNF, and FNF were studied by XRD, as shown in Fig. 4. All the pristine and doped NiO samples exhibit polycrystalline structures, which belong to the space group of *Fm3m* face-centered cubic (FCC) NiO phase (JCPDS# 47–1049). The peaks for ITO are labelled with an asterisk *. The XRD pattern reveals that the UNF sample has four diffraction peaks at 37.8°, 43.8°, 63.3°, and 75.8°, corresponding to (111), (200), (220), and (311) orientations,

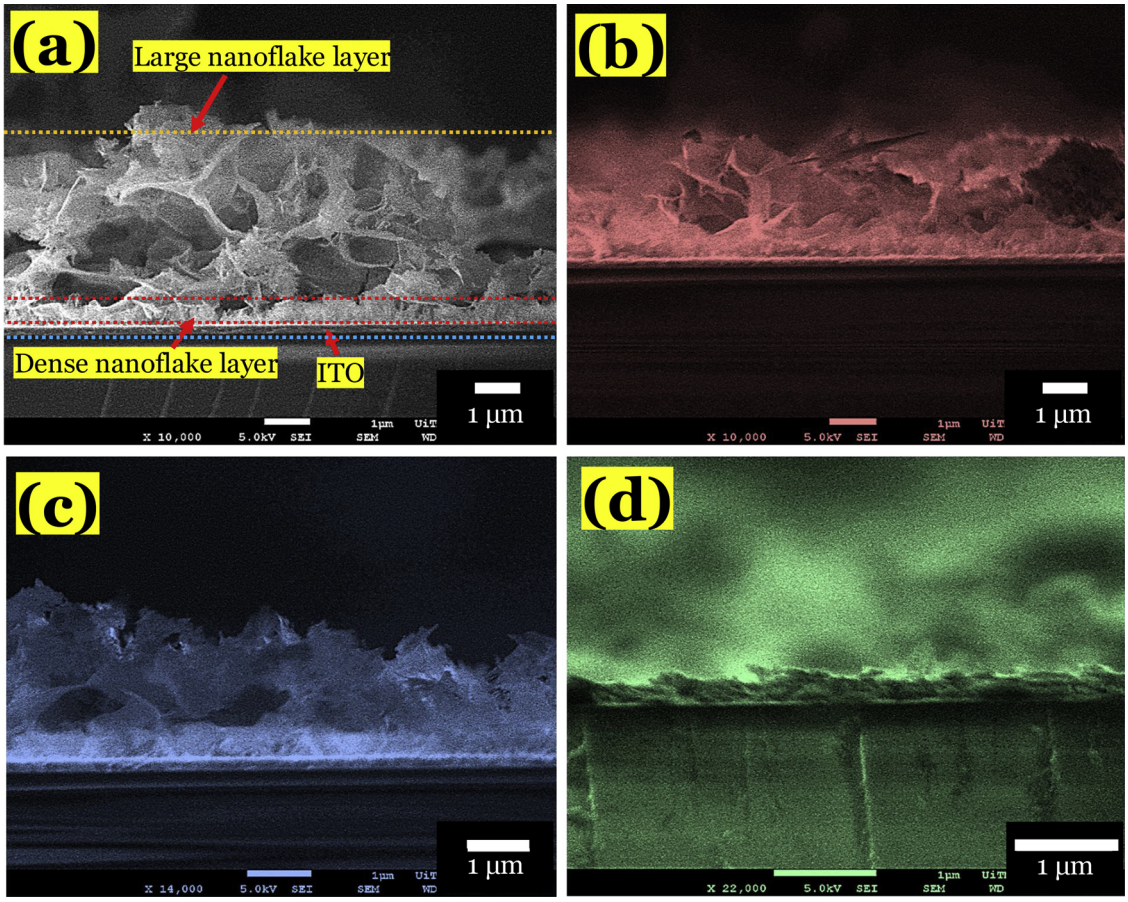


**Fig. 2.** Cross-sectional images of (a) UNF, (b) ZNF, (c) SNF, and (d) FNF samples.

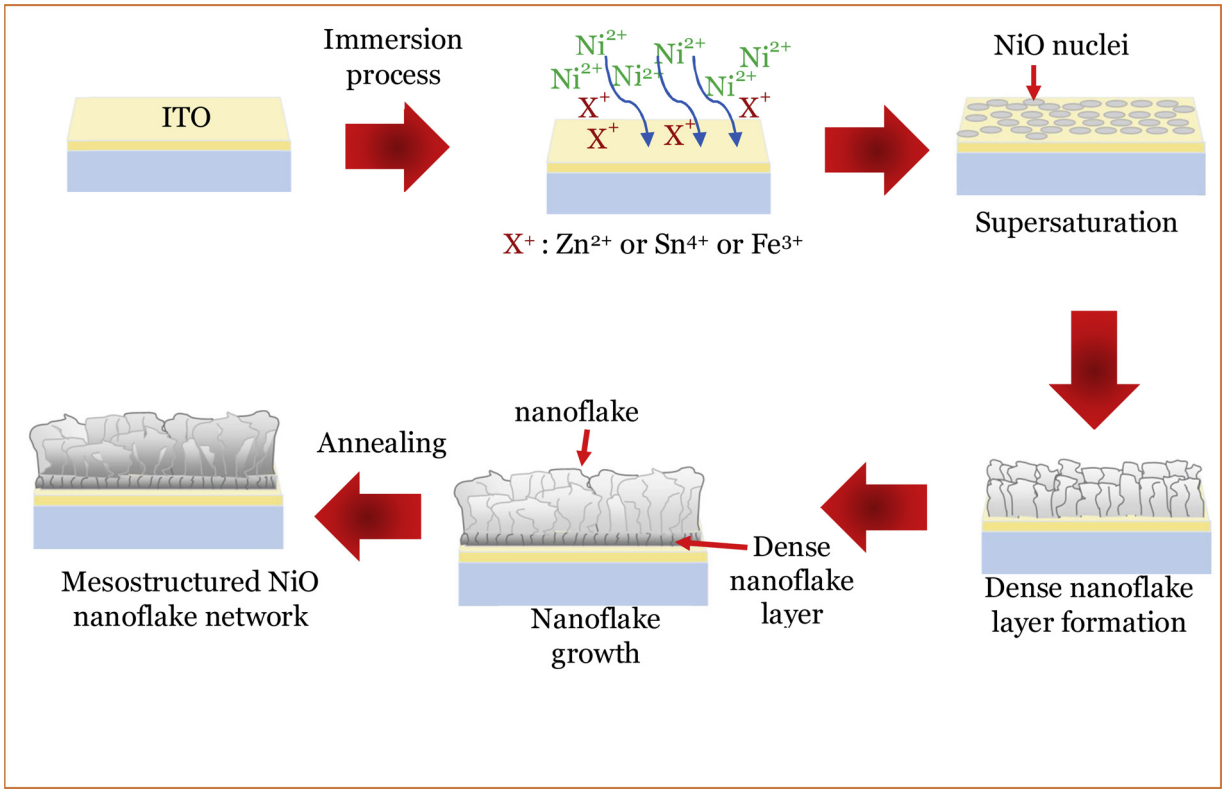


**Fig. 3.** Schematic growth mechanism of mesostructured NiO nanoflake network film on ITO glass.

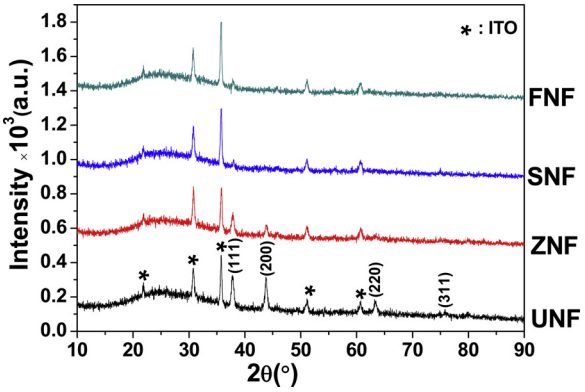


**Fig. 4.** X-ray diffraction patterns of UNF, ZNF, SNF, and FNF.

respectively. The pristine UNF sample shows sharp and clear diffraction peaks demonstrating a good crystalline quality. However, the intensities of these peaks was reduced significantly when the NiO samples were doped with Zn, Sn, and Fe sources. The shift of the Bragg angles $\theta$, to higher-angles, was observed for the XRD peaks with the addition of dopants. These angle shifts show that interactions take place between the dopants and Ni in the lattice due their electronegativity differences (Zn: 1.65 Pauling, Sn: 1.96 Pauling, Fe: 1.83 Pauling, Ni: 1.91 Pauling); this corroborates the integration of the dopants into the NiO lattice. This positive shift of diffraction peaks for the doped NiO samples also denotes the change of lattice parameters to lower values, revealing the fractional assimilation of dopant ions into the NiO lattice. For the doped samples, the FWHM of the XRD peaks were also broadened, which is due to the substitution of randomly localized dopant ions at the $Ni^{2+}$ sites in the NiO lattice. These dopant ions interrupt the equilibrium of the system and transform the properties of NiO. These results indicate that the crystallinity of the sample reduces after the doping process. This decline in crystallinity with addition of dopants is in agreement with the knowledge that the crystal growth could be inhibited due to the integration of dopants into the NiO lattice [30].

Scherrer's formula was applied to estimate the crystallite size $D$ from the (111) peak as shown by the following equation [31, 32]:

$$D = \frac{K\lambda}{\beta \cos\theta} \tag{6}$$

where $K$ represents a constant, given as 0.9, while λ is the XRD's X-ray wavelength (i.e., 1.5418 Å). Meanwhile, $\theta$ denotes the diffraction angle and $\beta$ refers to full-width at the half maximum (FWHM), which correlates with the diffraction broadening due to the dimensions of the crystallite. The crystallite sizes of the prepared samples are shown in Table 1. The crystallite sizes at different plane orientations, namely (200), (220), and (311), were also estimated based on the Scherrer formula and are tabulated in Table 2. However, the crystallite size based on the (220) and (311) planes for the ZNF sample could not be obtained due to the absence of these plane peaks in the XRD pattern. Meanwhile, for the SNF and FNF samples, the crystallite size based on other planes, except the (111) plane, could not be estimated due to the absence of other plane peaks in the XRD pattern, as can be observed in Fig. 4.

**Table 2**
Crystallite size of UNF, ZNF, SNF, and FNF calculated using Scherrer's formula at different planes.

| Sample | Crytallite size, D (nm) | | | | |
|---|---|---|---|---|---|
| | (111) | (200) | (220) | (311) | Average |
| UNF | 22.2 | 22.8 | 20.4 | 15.8 | 20.3 |
| ZNF | 20.1 | 19.9 | – | – | 20.0 |
| SNF | 16.1 | – | – | – | 16.1 |
| FNF | 13.8 | – | – | – | 13.8 |

The crystallite size was found to decrease with the introduction of dopants as in ZNF, SNF, and FNF samples. The reduced crystallite size of the doped samples shows that the growth of the host lattice was constrained by the dopant ions. These results support our previous discussion of the FESEM images regarding the inhibition of nanoflake growth with the addition of dopants. The NiO nanocrystals were prevented from developing and combining into larger crystals with the introduction of dopants. As a result, the nucleation and the successive growth rate of the doped NiO nanoflakes are reduced. These observations have also been reported in other works [33,34].

The lattice constant $a$, of cubic NiO structure, and the interplanar spacing of the diffraction planes $d$, were deduced for the crystalline plane of (111) using the following Bragg equations:

$$a = d\sqrt{h^2 + k^2 + l^2} \tag{7}$$

$$d = \frac{n\lambda}{2\sin\theta} \tag{8}$$

where $h$, $k$, and $l$ denote the Miller indices of the (111) planes, while λ represents the X-ray wavelength. In this equation, $\theta$ is the diffraction angle of (111) plane and $n$ refers to the value for order of diffraction, which is normally given as 1. The lattice constant $a$, and the interplanar spacing $d$, for the UNF, ZNF, SNF, and FNF are presented in Table 1. From the values obtained, it can be seen that lattice shrinkage is observed for all samples as compared to that of the bulk NiO (4.1771 Å), which could be attributed to the Ni vacancies and dopant integration into the NiO lattice [35]. The reduced lattice parameters $a$ and interplanar spacing $d$, with introduction of Zn, Sn, and Fe dopants, are revealing of the cell volume narrowing and structural distortion induced by strain/stress. The unit cell volume can be estimated by the relation:

$$V = a^3 \tag{9}$$

where $a$ represents the lattice constant. The calculated cell volumes of the samples are shown in Table 1. The strain $S$ values for UNF, ZNF, SNF, and FNF developed along the a-axis were calculated as follows:

$$S = \frac{a - a_0}{a_0} \times 100 \tag{10}$$

where, $a_o$ represents the lattice parameter of standard bulk NiO films (0.4177 nm). The positive and negative value of strain denotes the

**Table 1**
FWHM, lattice parameter, unit cell volume, crystallite size, interplanar spacing, Dislocation density, stress, and strain values of undoped and doped NiO nanoflake network films.

| Samples | FWHM $\beta$ (°) | Lattice parameter $a$ (nm) | Unit cell volume $V$ ($10^{-2}\times nm^3$) | Crystallite size $D$ (nm) | Interplanar spacing $d$ (nm) | Dislocation density $\delta$ ($\times 10^{15}$ Lines/$m^2$) | Stress $\sigma$ (GPa) (positive sign denotes tensile stress) | Strain $S$ (%) (negative sign denotes compressive strain) |
|---|---|---|---|---|---|---|---|---|
| UNF | 0.395 | 0.4121 | 7.00 | 22.2 | 0.2379 | 6.09 | 4.32 | −1.34 |
| ZNF | 0.435 | 0.4119 | 6.99 | 20.1 | 0.2378 | 7.43 | 4.44 | −1.38 |
| SNF | 0.545 | 0.4112 | 6.95 | 16.1 | 0.2374 | 11.57 | 5.03 | −1.56 |
| FNF | 0.636 | 0.4103 | 6.91 | 13.8 | 0.2369 | 15.75 | 5.73 | −1.78 |

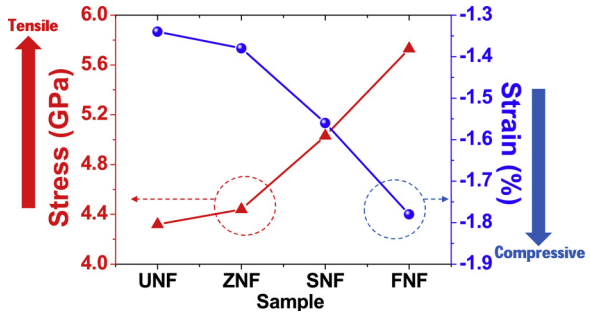


**Fig. 5.** Strain and stress of NiO nanoflake network films doped with different sources of Zn, Sn, and Fe.

tensile strain (positive) and compressive strain (negative), respectively. The tensile strain indicates that the material is being stretched along the a-axis, while the compressive stress refers to the material that is being compressed to the a-axis. All samples exhibited compressive strain with the values increasing according to the order: UNF < ZNF < SNF < FNF. Then, the residual stress of the undoped and doped samples was studied. The stress $\sigma$ of the sample grown on the ITO substrate is expressed by following relation [36,37]:

$$\sigma = \frac{-E(a - a_o)}{2pa_o} \tag{11}$$

Here, $a_o$ denotes the lattice parameter of standard bulk NiO films, which is given as 0.4177 nm. The $p$ and $E$ refer to Poisson ratio ($p$ = 0.31) and Young's modulus ($E$ = 200 GPa) of NiO, respectively [36, 37]. The calculation results are summarized in the Table 1, which indicates that all samples exhibit tensile stress (all stress values are positive). The strain and stress correlation of the UNF, ZNF, SNF, and FNF samples are shown in Fig. 5. The change of the lattice constant to a lower value reflects the higher tensile stress conditions for the synthesized samples.

This results reinforce the augmented pattern of tensile strain and FWHM for the UNF followed by the ZNF, SNF, and FNF samples. It has been reported that oxygen interstitial defects could induced the presence of stress in the films [38]. In this work, all films were grown using an aqueous solution which facilitates an oxygen-rich environment. Therefore, the formation of oxygen interstitials could not be neglected. According to Kim et al., under the presence of oxygen interstitials or adsorbed oxygen ions, $Ni^{2+}$ ions in NiO could oxidize into $Ni^{3+}$ to increase the $Ni^{3+}/Ni^{2+}$ ratio [39]. In their analysis, they found that the addition of Sn dopant increases the $Ni^{3+}/Ni^{2+}$ ratio. Consequently, this high $Ni^{3+}/Ni^{2+}$ ratio induces the increase of negatively charged oxygen species at the NiO surface, or inside the NiO lattice, according to the following equation:

$$\frac{1}{2}O_2 + 2NiO \xrightarrow{2NiO} O''_{surf}(or \cdot O_i'') + 2Ni_{Ni}^{\bullet} + 2O_O^{\times} \tag{12}$$

The increased $Ni^{3+}/Ni^{2+}$ ratio has also been reported for Fe doped NiO [40]. Similarly, Wang et al. reported that the deposited Zn-doped NiO films displayed oxygen-rich stoichiometric properties [41].

The stress and strain in the lattice can generate both physical and dislocation defects in the NiO films. The dislocation density $\delta$ of the undoped and doped samples can be calculated using following equation [42]:

$$\delta = \frac{3}{D^2} \tag{13}$$

where $D$ refers to the crystallite size estimated from the Scherrer formula. The calculation results show that UNF, ZNF, SNF, and FNF have dislocation densities of 6.09 × $10^{15}$, 7.43 × $10^{15}$, 11.57 × $10^{15}$, and 15.75 × $10^{15}$ lines/$m^2$, respectively. The dislocation density of ZNF, SNF, and FNF increased due to the doping process as a result of lattice imperfections.

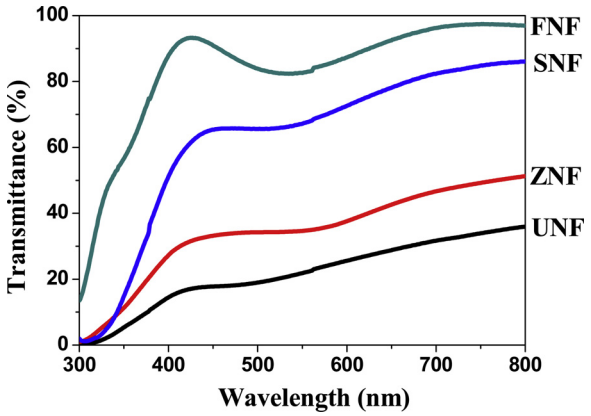


**Fig. 6.** Transmittance spectra of UNF, ZNF, SNF, and FNF films.

The optical transmittance spectra of UNF, ZNF, SNF, and FNF are shown in Fig. 6. The spectra indicate that the samples have transparency in the visible region, with average values of 26 %, 40 %, 73 %, and 91 %, for UNF, ZNF, SNF, and FNF, respectively. However, the spectra show that all samples have an onset of fundamental absorption in the UV region at a wavelength below 400 nm. This fundamental absorption shows a blue-shift with the addition of dopants. The modifications in the fundamental absorption after the doping process are an indication of dopant incorporation in the NiO lattice, which changes the gap states.

For a direct band gap semiconductor material, the parabolic band gap energy $E_g$ and absorption coefficient $\alpha$, can be linked by the following equation:

$$ahv = A(hv - E_g)^{1/2} \tag{14}$$

where $A$ denotes a constant, while $h\nu$ represents the photon energy. The band gap energy of the samples can be estimated by plotting $(\alpha h\nu)^2$ against the $h\nu$, where the extrapolated linear line of this plot at the $h\nu$ axis gives the band gap of the samples. The estimated $E_g$ values from the Tauc plot in Fig. 7 for UNF, ZNF, SNF, and FNF samples are summarized in Table 3.

The strain/stress in the film is one of the important factors that affect the band gap of a semiconductor. The higher tensile strain or compressive stress in the film will produce a lower band gap energy, whereas the higher compressive strain or tensile stress will induce a higher band gap energy of the semiconductor material [43]. The ZNF film exhibits a slightly higher compressive strain and tensile stress value, as compared to UNF film, which may explain the increment of the band gap of the ZNF. Similarly, the SNF and FNF samples have larger compressive strain and tensile stress than that of the UNF and ZNF, which can be correlated with the blue shift in the optical band gap of these samples. According to this result, the band gap values of the sample are UNF < ZNF < SNF < FNF. This ordering also reflects the lattice contraction as discussed in the XRD analysis. Ghosh et al. reported that the shrinkage of the lattice causes the band gap broadening of the samples [44]. The shrinkage of the lattice size provides a broader band gap because of the augmented repulsion between the Ni 3d and O 2p orbitals. According to Dewan et al., the band gap energy of the doped NiO film can be also be influenced by oxygen vacancy defects [37]. The oxygen vacancy defects could form extra defect states in the forbidden region between valence band and conduction band, which may reduce the band gap of the films. The shift of the band gap energy may be affected by the delocalization state at the edge of the conduction band, which facilitates shallow traps or deep traps in the electronic band. Carbone et al. reported that the band gap energy of the samples is also influenced by the thinness and porosity of the samples [45]. These conditions provide defect states at the internal hole boundaries, which affects the band gap. The thin and dense samples tend to have larger

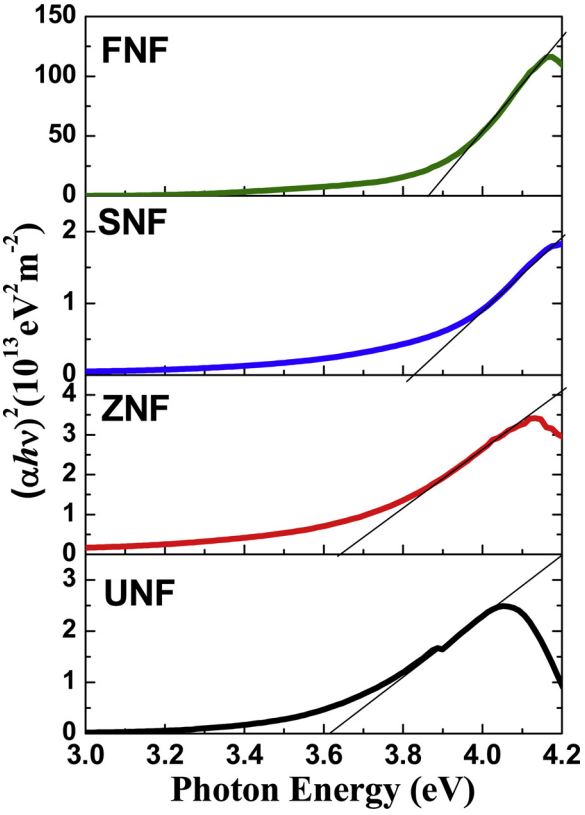


**Fig. 7.** Plot of $(ahv)^2$ versus the photon energy $hv$ for UNF, ZNF, SNF, and FNF to determine optical band gap.

band gaps. In their study, Akaltun et al. reported that thin NiO tends to exhibit larger bandgaps due to changes in crystal structure, morphology, atomic distance, grain size, and structural defects in the films [46].

The refractive index $n$ values for the UNF, ZNF, SNF, and FNF samples were estimated using the Moss relation, which has a direct correlation with the optical band gap energy. The formula is given below [46–48]:

$$n = \left(\frac{k}{E_g}\right)^{1/4} \tag{15}$$

Here, $k$ denotes a constant with a given value of 108 eV. The refractive index $n$ can also be estimated using a different equation suggested by Herve and Vandamme, as shown below [49–51]:

$$n = \sqrt{1 + \left(\frac{A}{B + E_g}\right)^2} \tag{16}$$

where $A$ is the hydrogen ionization energy with a value of 13.6 eV, while $B$ is a constant related to UV resonance energy and band gap energy difference with a value of 3.4 eV. The refractive index, $n$ is regarded as one of the important characteristics of a material, which provides information about the electronic polarizability of ions, and the local field inside a particular material. The refractive index n values of these samples, using both relations, are summarized in Table 3. Both relations suggest that the sample with a higher band gap energy has a lower value of refractive index $n$.

Based on the refractive index $n$ obtained from both the Moss and the Herve and Vandamme relations, the high frequency dielectric constant, $\varepsilon_\infty$ values for the UNF, ZNF, SNF, and FNF samples were deduced from the following relation [47]:

$$\varepsilon_\infty = n^2 \tag{17}$$

where $n$ refers to the refractive index. Then, the static dielectric constant $\varepsilon_o$ of the undoped and doped films was estimated using the following equation, which shows the energy band gap dependence $\varepsilon_o$ for semiconductors compounds: [49].

$$\varepsilon_o = 18.52 - 3.08E_g \tag{18}$$

For different dopants the estimated $\varepsilon_\infty$ and $\varepsilon_o$ values of the samples are summarized in Table 3. The results show that UNF has the highest $\varepsilon_\infty$ and $\varepsilon_o$ values, followed by the ZNF, SNF, and FNF samples.

The room temperature Raman spectra for UNF, ZNF, SNF, and FNF samples are shown in Fig. 8. This analysis was conducted to assess the effects of dopants on the structural variations of the nanoflake network films. There are four Raman peaks observed in the UNF sample, which are assigned to one-phonon transverse optical mode (TO) at 461 $cm^{-1}$, one-phonon longitudinal optical (LO) mode at 496 $cm^{-1}$, two-phonon 2TO stretching modes at 789 $cm^{-1}$, and two-phonon 2LO phonon modes located at 1093 $cm^{-1}$ [52]. The ZNF, SNF, and FNF samples also exhibit these Raman peaks and their peak positions are summarized in the Table 4. According to previous studies, the first order Raman scattering of 1TO and 1LO are normally absent for cubic or rhombohedral NiO with perfect stoichiometry [53,54]. However, in our work, these peaks appeared in the Raman spectra which indicate the existence of structural disorders in the grown nanoflake structure, which include nickel vacancies, oxygen interstitials, and surface effects [30]. Broader 1TO and 1LO peaks could be observed for the doped samples of ZNF, SNF, and FNF, in which the peak positions are shifted towards a higher wavenumber of the Raman shift, as compared to the pristine UNF sample. This shift to the higher Raman wavenumbers could also be observed in the case of 2TO and 2LO vibration modes. These changes are caused by lattice defects induced by the dopant incorporation into the NiO lattice in order to conserve the charge neutrality in the structure [30]. These defects result in the shrinkage of both lattice parameters and unit cell volume, as previously discussed in the XRD patterns. Subsequently, the bond length decreases which leads to the improvement of the force constant. As a result, the vibration frequency, or wavenumber, of the Raman shift moves towards a higher value.

The one-phonon 1LO vibration peak is also associated with Ni vacancy defects and the incidence of $Ni^{3+}$ ions [55–58]. The reduced intensity of the one-phonon 1LO after doping with Zn, Sn, and Fe indicates that the Ni vacancy defects are reduced in the doped samples. The dopants might occupy the vacancy sites to reduce the Ni vacancy defects in the process. In addition, the reduced intensity of this Raman

**Table 3**
Optical properties of NiO nanoflake network films doped with Zn, Sn, and Fe.

| Sample | Optical bandgap $E_g$ (eV) | Static dielectric constant $\varepsilon_o$ | Moss relation | | Herve and Vandamme relation | |
|---|---|---|---|---|---|---|
| | | | Refractive index $n$ | High frequency dielectric constant $\varepsilon_\infty$ | Refractive index $n$ | High frequency dielectric constant $\varepsilon_\infty$ |
| UNF | 3.61 | 7.40 | 2.34 | 5.47 | 2.18 | 4.76 |
| ZNF | 3.67 | 7.22 | 2.33 | 5.42 | 2.17 | 4.70 |
| SNF | 3.83 | 6.72 | 2.30 | 5.31 | 2.13 | 4.54 |
| FNF | 3.86 | 6.63 | 2.30 | 5.29 | 2.12 | 4.51 |

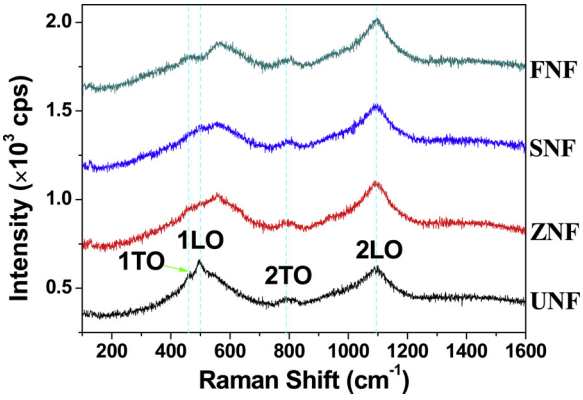


**Fig. 8.** Raman spectra of undoped NiO nanoflake network film and the films doped with Zn, Sn, and Fe.

**Table 4**
Raman peak positions for UNF, ZNF, SNF, and FNF samples.

| Sample | 1LO Peak ($cm^{-1}$) | 1TO Peak ($cm^{-1}$) | 2TO Peak ($cm^{-1}$) | 2LO Peak ($cm^{-1}$) |
|---|---|---|---|---|
| UNF | 461 | 496 | 789 | 1094 |
| ZNF | 463 | 557 | 792 | 1096 |
| SNF | 464 | 559 | 794 | 1097 |
| FNF | 467 | 562 | 803 | 1098 |

peak for the doped samples is attributed to the inhibition of the nanoflake growth after the doping process. Meanwhile, the shift of the 1LO peak to higher Raman wavenumbers, for the doped samples, is contributed by the substitution of dopant ions with higher oxidation states than $Ni^{2+}$ [40,59]. The shift was more pronounced for FNF, follow by SNF and ZNF. The doped samples also show a strong 2LO phonon mode in comparison with the pristine UNF, which is attributed to the vibration of Ni-O bond. In the meantime, a broad two-phonon 2TO Raman mode, with low intensity, appeared for all doped samples. However, the two-magnon (2 M) vibration mode, which normally appears in the Raman spectra of bulk NiO at 1490 $cm^{-1}$ and involves interaction between the phonon and Brillouin zone-edge magnons, is not present in our samples [60,61]. These results suggest that the antiferromagnetic spin correlations are decreased in these samples due to the smaller crystallites and induced structural disorder. Subsequently, the transition of antiferromagnetic-to-paramagnetic properties occurred in our samples.

The I–V measurement plots of UNF, ZNF, SNF, and FNF samples are shown in Fig. 9. All samples exhibit the Ohmic characteristic, as linear plots that obey Ohm`s law were obtained. The results indicate that the current value, with respect to the supplied voltage for the doped

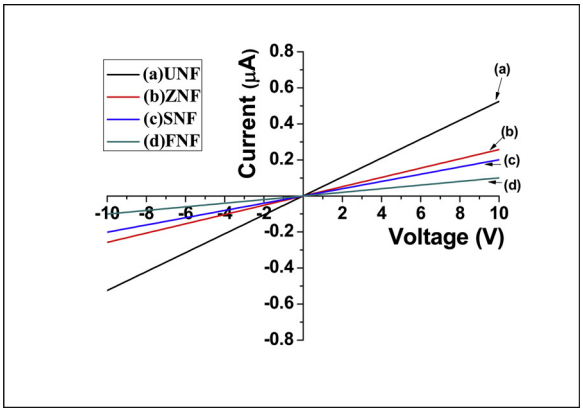


**Fig. 9.** I-V plots of UNF, ZNF, SNF, and FNF samples.

samples, decrease according to the following sequence: UNF > ZNF > SNF > FNF. Subsequently, the resistivity ρ of UNF, ZNF, SNF, and FNF samples was calculated from the I–V measurement plots using equation:

$$\rho = \left(\frac{V}{I}\right)\frac{A}{t} \tag{19}$$

where $V/I$, $A$, and $t$ represent the reciprocal of the I–V plot gradient (or resistance), surface area of the contacts, and film thickness, respectively. The calculated resistivity of the UNF, ZNF, SNF, and FNF samples are 4.08 × $10^7$, 9.98 × $10^7$, 2.13 × $10^8$, and 3.58 × $10^9$ Ω·m, respectively. These results show that the resistivity of the NiO nanoflake network film increases when doped with Zn, Sn, and Fe, as compared to that of UNF, which suggests that the hole concentrations of the doped samples are reduced through an electronic compensation mechanism [30]. On the other hand, the resistivity for the FNF sample was the highest among the doped samples, which could be attributed to the FNF film's characteristics that are structurally inferior, as discussed previously. This could possibly result in inferior charge transport properties [62]. The integration of Fe dopants with high density in the NiO lattice could also reduce the hole concentration in the film. This condition reduces the conduction of the FNF film. Meanwhile, the SNF and ZNF possess lower resistivity than that of FNF, due to their superior structural properties, which enhances the charge conduction across the films.

In general, native NiO exhibits p-type conductivity due to the formation of microstructural defects such as Ni vacancies, which cause off-stoichiometric characteristics of this material. The Ni vacancy defects could form in the lattice during the thermal process when the nanostructures react with oxygen, as shown by the following [37]:

$$\frac{1}{2}O_2 \leftrightarrow O_O + V_{Ni}^{-} + h^{+} \tag{20}$$

The singly ionized Ni vacancy is considered in this reaction to conserve the charge neutrality of the NiO. Throughout this reaction, the hole (positively charged) is formed together with a singly ionized Ni vacancy (negatively charged). This equation indicates that the Ni vacancy defect is created in the NiO lattice, which produces electrical conductivity through hole conveyance.

The metal doping in NiO could be actualized through the substitution of metal doping X (Zn, Sn, or Fe dopants) at the $Ni^{2+}$ site. This substitution engenders electrons by the electronic compensation mechanism, as can be denoted by the following equation [33]:

$$X_m O_n \xrightarrow{mNiO} mX_{Ni}^{\bullet} + (n-1)O_O^{\times} + \frac{1}{2}O_2 + me^{-} \tag{21}$$

where X is the dopant ion. Therefore, for Zn, Sn, and Fe dopants, the equations could be simplified as below:

$$\textit{ForZn doping: } ZnO \xrightarrow{NiO} Zn_{Ni}^{\bullet} + \frac{1}{2}O_O^{\times} + \frac{1}{2}O_2 + e^{-} \tag{22}$$

$$\textit{For Sn doping: } SnO_2 \xrightarrow{NiO} Sn_{Ni}^{\bullet} + O_O^{\times} + \frac{1}{2}O_2 + e^{-} \tag{23}$$

$$\textit{For Fe doping: } \frac{1}{2}Fe_2O_3 \xrightarrow{NiO} Fe_{Ni}^{\bullet} + O_O^{\times} + \frac{1}{2}O_2 + e^{-} \tag{24}$$

The generated electrons in the doping process reduces the hole concentration in the p-type NiO. Accordingly, the resistivity of the doped samples increases, which is attributed to the decreased hole concentration through the electronic compensation mechanism.

## 4. Conclusion

Mesostructured NiO nanoflake network films doped with Zn, Sn, and Fe were prepared by solution immersion and their optical and structural characteristics were investigated. The growth mechanism of mesostructured NiO nanoflake network films on ITO glass is proposed. Upon doping NiO with Zn, Sn, and Fe sources, the films exhibit dense

morphologies with small nanoflake network structures and reduced thicknesses. The crystalline properties of the doped samples also deteriorated, which signifies the incorporation of dopants into the NiO lattice. The doped samples showed a reduced lattice parameter, crystallite size, interplanar spacing, and unit cell volume, according to the following sequence: UNF > ZNF > SNF > FNF. In addition, the doped samples also exhibited high dislocation density, compressive strain, tensile stress, and optical band gap, where the increase of these characteristics was most pronounced for the Fe-doped, followed by the Sn-doped, Zn-doped, and undoped samples. The formation of structural disorder in NiO after the doping process was confirmed from the Raman spectra analysis. The resistivity of the NiO films increased after doping with Zn, Sn, and Fe, which was attributed to the electronic compensation mechanism. These characteristic deviations of the NiO nanoflake network film doped with different metal sources are very useful for different kinds of applications.

## Author agreement

Submission of work requires that the piece to be reviewed has not been previously published. Upon acceptance, the Author assigns to the Materials Research Bulletin the right to publish and distribute the manuscript in part or in its entirety. The Author's name will always be included with the publication of the manuscript.

The Author has the following nonexclusive rights: (1) to use the manuscript in the Author's teaching activities; (2) to publish the manuscript, or permit its publication, as part of any book the Author may write; (3) to include the manuscript in the Author's own personal or departmental (but not institutional) database or on-line site; and (4) to license reprints of the manuscript to third persons for educational photocopying. The Author also agrees to properly credit the Optical Materials as the original place of publication.

The Author hereby grants the Materials Research Bulletin full and exclusive rights to the manuscript, all revisions, and the full copyright. The Materials Research Bulletin rights include but are not limited to the following: (1) to reproduce, publish, sell, and distribute copies of the manuscript, selections of the manuscript, and translations and other derivative works based upon the manuscript, in print, audio-visual, electronic, or by any and all media now or hereafter known or devised; (2) to license reprints of the manuscript to third persons for educational photocopying; (3) to license others to create abstracts of the manuscript and to index the manuscript; (4) to license secondary publishers to reproduce the manuscript in print, microform, or any computer-readable form, including electronic on-line databases; and (5) to license the manuscript for document delivery. These exclusive rights run the full term of the copyright, and all renewals and extensions thereof. I hereby accept the terms of the above Author Agreement.

## Declaration of Competing Interest

None.

## Acknowledgement

This research was conducted under the ASEAN-India Research & Training Fellowship Scheme (IMRC/AISTDF/R&D/P-1/2017). This research was supported by Fundemental Research Grant Scheme (FRGS) (File No: FRGS/1/2018/TK04/UITM/02/23). The authors would like to acknowledge the Faculty of Electrical Engineering and Institute of Research Management and Innovation (IRMI) of UiTM for their support.

## Appendix A. Supplementary data

Supplementary material related to this article can be found, in the online version, at doi:https://doi.org/10.1016/j.materresbull.2020.110860.

## References

[1] M. Ben Amor, A. Boukhachem, A. Labidi, K. Boubaker, M. Amlouk, J. Alloys. Compd. 693 (2017) 490–499.
[2] W. Sun, L. Xiao, X. Wu, J. Alloys. Compd. 772 (2019) 465–471.
[3] X. Yin, J. Zhai, T. Wang, W. Jing, L. Song, J. Xiong, Mater. Lett. 231 (2018) 101–104.
[4] H. Ren, C. Gu, S.W. Joo, J. Zhao, Y. Sun, J. Huang, Sens. Actuators B Chem. 266 (2018) 506–513.
[5] M.A.R. Abdullah, M.H. Mamat, A.S. Ismail, M.F. Malek, A.B. Suriani, M.K. Ahmad, I.B. Shameem Banu, R. Amiruddin, M. Rusop, Mater. Lett. 236 (2019) 460–464.
[6] B. Liu, M. Wang, S. Liu, H. Zheng, H. Yang, Sens. Actuators B Chem. 273 (2018) 794–803.
[7] Q. Zheng, Y. Liu, H. Guo, X. Hua, S. Shi, M. Zuo, Mater. Res. Bull. 98 (2018) 155–159.
[8] R. Chouhan, P. Baraskar, A. Agrawal, M. Gupta, P. Sen, Opt. Mater. (Amst) 84 (2018) 893–898.
[9] Z. Mehraban, F. Farzaneh, A. Shafiekhani, Opt. Mater. (Amst) 29 (2007) 927–931.
[10] E.A. Rogozea, N.L. Olteanu, A.R. Petcu, C.A. Lazar, A. Meghea, M. Mihaly, Opt. Mater. (Amst) 56 (2016) 45–48.
[11] D.K. Pathak, A. Chaudhary, S. Mishra, P. Yogi, S.K. Saxena, P.R. Sagdeo, R. Kumar, Superlattices Microstruct. 125 (2019) 138–143.
[12] H. Zhou, B. Lv, Y. Xu, D. Wu, Mater. Res. Bull. 50 (2014) 399–404.
[13] S.R. Gawali, V.L. Patil, V.G. Deonikar, S.S. Patil, D.R. Patil, P.S. Patil, J. Pant, J. Phys. Chem. Solids 114 (2018) 28–35.
[14] Q. Li, C.-L. Li, Y.-L. Li, J.-J. Zhou, C. Chen, R. Liu, L. Han, Inorg. Chem. Commun. 86 (2017) 140–144.
[15] A. Diha, S. Benramache, B. Benhaoua, Optik 172 (2018) 832–839.
[16] C. Feng, X. Kou, B. Chen, G. Qian, Y. Sun, G. Lu, Sens. Actuators B Chem. 253 (2017) 584–591.
[17] L.S. Nair, D. Chandran, V.M. Anandakumar, K. Rajendra Babu, Ceram. Int. 43 (2017) 11090–11096.
[18] K.N. Patel, M.P. Deshpande, V.P. Gujarati, S. Pandya, V. Sathe, S.H. Chaki, Mater. Res. Bull. 106 (2018) 187–196.
[19] S. Wang, D. Huang, S. Xu, W. Jiang, T. Wang, J. Hu, N. Hu, Y. Su, Y. Zhang, Z. Yang, J. Chem. Soc. Faraday Trans. 19 (2017) 19043–19049.
[20] X. Sun, X. Hu, Y. Wang, R. Xiong, X. Li, J. Liu, H. Ji, X. Li, S. Cai, C. Zheng, J. Phys. Chem. C 119 (2015) 3228–3237.
[21] R. Lontio Fomekong, H.M. Tedjieukeng Kamta, J. Ngolui Lambi, D. Lahem, P. Eloy, M. Debliquy, A. Delcorte, J. Alloys. Compd. 731 (2018) 1188–1196.
[22] R. Sharma, A.D. Acharya, S.B. Shrivastava, M.M. Patidar, M. Gangrade, T. Shripathi, V. Ganesan, Optik 127 (2016) 4661–4668.
[23] C. Mallika, A.M. Edwin Suresh Raj, K.S. Nagaraja, O.M. Sreedharan, Thermochim. Acta 371 (2001) 95–101.
[24] M. Masoumi, D.M. Cupid, T.L. Reichmann, K. Chang, D. Music, J.M. Schneider, H.J. Seifert, Int. J. Mater. Res. 108 (2017) 869–878.
[25] S. Phapale, R. Mishra, D. Das, J. Nucl. Mater. 373 (2008) 137–141.
[26] S.Y. Kuo, W.C. Chen, F.I. Lai, C.P. Cheng, H.C. Kuo, S.C. Wang, W.F. Hsieh, J. Cryst. Growth 287 (2006) 78–84.
[27] J. Rouhi, M.H. Mamat, C.H.R. Ooi, S. Mahmud, M.R. Mahmood, PLoS One 10 (2015) e0123433.
[28] M. Alimanesh, Z. Hassan, N. Zainal, Opt. Mater. (Amst) 72 (2017) 276–282.
[29] H. Jiang, T. Zhao, C. Li, J. Ma, J. Mater. Chem. 21 (2011) 3818–3823.
[30] Z. Wang, H. Zhou, D. Han, F. Gu, J. Mater. Chem. C 5 (2017) 3254–3263.
[31] P. Scherrer, Nachrichten von der Gesellschaft der Wissenschaften, Göttingen, Mathematisch-Physikalische Klasse 2 (1918) 98.
[32] A.L. Patterson, Phys. Rev. 56 (1939) 978–982.
[33] C. Wang, J. Liu, Q. Yang, P. Sun, Y. Gao, F. Liu, J. Zheng, G. Lu, Sens. Actuators B Chem. 220 (2015) 59–67.
[34] H. Gao, Q. Yu, S. Zhang, T. Wang, P. Sun, H. Lu, F. Liu, X. Yan, F. Liu, X. Liang, Y. Gao, G. Lu, Sens. Actuators B Chem. 269 (2018) 210–222.
[35] Y.H. Lin, J. Wang, J. Cai, M. Ying, R. Zhao, M. Li, C.W. Nan, Phys. Rev. B 73 (2006) 193308.
[36] A. Mallikarjuna Reddy, A. Sivasankar Reddy, P. Sreedhara Reddy, Vacuum 85 (2011) 949–954.
[37] S. Dewan, M. Tomar, R.P. Tandon, V. Gupta, J. Appl. Phys. 121 (2017) 215307.
[38] V. Gupta, A. Mansingh, J. Appl. Phys. 80 (1996) 1063–1073.
[39] B.Y. Kim, J.W. Yoon, J.K. Kim, Y.C. Kang, J.H. Lee, ACS Appl. Mater. Interfaces 10 (2018) 16605–16612.
[40] L. Xiu, T. Jian-Feng, E.H. Yan, H. Xin-Tang, Mater. Res. Express 4 (2017) 045015.
[41] J. Wang, X. Wei, P. Wangyang, Nanoscale Res. Lett. 10 (2015) 461.
[42] G.K. Williamson, R.E. Smallman, Philos. Mag. 1 (1956) 34–46.
[43] A. Yazdani, H. Zafarkish, K. Rahimi, Mater. Sci. Semicond. Process. 74 (2018) 225–231.
[44] R. Ghosh, D. Basak, S. Fujihara, J. Appl. Phys. 96 (2004) 2689–2692.
[45] M. Carbone, E. Maria Bauer, L. Micheli, M. Missori, Colloids Surf. A Physicochem. Eng. Asp. 532 (2017) 178–182.
[46] Y. Akaltun, T. Çayır, J. Alloys. Compd. 625 (2015) 144–148.
[47] L. Hannachi, N. Bouarissa, Physica B Condens. Matter 404 (2009) 3650–3654.
[48] V.P. Gupta, N.M. Ravindra, Phys. Status Solidi B 100 (1980) 715–719.
[49] F. Mezrag, W. Kara Mohamed, N. Bouarissa, Physica B Condens. Matter 405 (2010)

2272–2276.
[50] S.K. Tripathy, Opt. Mater. (Amst) 46 (2015) 240–246.
[51] P. Hervé, L.K.J. Vandamme, Infrared Phys. Technol. 35 (1994) 609–615.
[52] P. Bose, S. Ghosh, S. Basak, M.K. Naskar, J. Asian Ceram. Soc. 4 (2016) 1–5.
[53] P. Ravikumar, B. Kisan, A. Perumal, AIP Adv. 5 (2015) 087116.
[54] S. Liu, J. Jia, J. Wang, S. Liu, X. Wang, H. Song, X. Hu, J. Magn. Magn. Mater. 324 (2012) 2070–2074.
[55] D.Y. Jiang, J.M. Qin, X. Wang, S. Gao, Q.C. Liang, J.X. Zhao, Vacuum 86 (2012) 1083–1086.
[56] C.A. Melendres, S. Xu, J. Electrochem. Soc. 131 (1984) 2239–2243.
[57] D.A. Wruck, M. Rubin, J. Electrochem. Soc. 140 (1993) 1097–1104.
[58] S.H. Lee, H.M. Cheong, N.G. Park, C.E. Tracy, A. Mascarenhas, D.K. Benson, S.K. Deb, Solid State Ion. 140 (2001) 135–139.
[59] Y. Ji-Wook, K. Hyo-Joong, K. Il-Doo, L. Jong-Heun, Nanotechnology 24 (2013) 444005.
[60] F.T. Thema, E. Manikandan, A. Gurib-Fakim, M. Maaza, J. Alloys. Compd. 657 (2016) 655–661.
[61] R.E. Dietz, G.I. Parisot, A.E. Meixner, Phys. Rev. B 4 (1971) 2302–2310.
[62] I. Fasaki, A. Koutoulaki, M. Kompitsas, C. Charitidis, Appl. Surf. Sci. 257 (2010) 429–433.